^<13>N-ammonia positron emission tomography-derived left ventricular strain in patients after heart transplantation validated using cardiovascular magnetic resonance feature tracking as reference

Kawakubo, Masateru
Department of Health Sciences, Faculty of Medical Sciences, Kyushu University

Nagao, Michinobu
Department of Diagnostic Imaging & Nuclear Medicine, Tokyo Women's Medical University

Kikuchi, Noriko
Department of Cardiology, Tokyo Women's Medical University

Yamamoto, Atsushi
Department of Diagnostic Imaging & Nuclear Medicine, Tokyo Women's Medical University

他

出版情報：Annals of nuclear medicine. 36 (1), pp.70-81, 2021-10-13. Japanese Society of Nuclear Medicine
バージョン：
権利関係：

^{13}N-ammonia positron emission tomography-derived left ventricular strain in patients after heart transplantation validated using cardiovascular magnetic resonance feature tracking as reference

Short title: PET-derived LV strain measurement

Type of article: Original article

Masateru Kawakubo, PhD[1], Michinobu Nagao, MD[2*], Noriko Kikuchi, MD[3], Atsushi Yamamoto, MD[2], Risako Nakao, MD[3], Yuka Matsuo, MD[2], Koichiro Kaneko, MD[2], Eri Watanabe, MD[3], Masayuki Sasaki, MD[1], Shinichi Nunoda, MD[4], and Shuji Sakai, MD[2]

[1] Department of Health Sciences, Faculty of Medical Sciences, Kyushu University, Fukuoka, Japan

[2] Department of Diagnostic Imaging & Nuclear Medicine, Tokyo Women's Medical University, Tokyo, Japan

[3] Department of Cardiology, Tokyo Women's Medical University, Tokyo, Japan

[4] Department of Therapeutic Strategy for Severe Heart Failure, Graduate School of Medicine, Tokyo Women's Medical University, Tokyo, Japan

Authors' ORCID iD:

Masateru Kawakubo: 0000-0003-1867-1745

Michinobu Nagao: 0000-0001-6049-8857

***Corresponding author**:

Michinobu Nagao, MD

Associate Professor, Department of Diagnostic Imaging & Nuclear Medicine, Tokyo Women's Medical University

8-1 Kawada-cho, Shinjuku-ku, Tokyo 162-8666, Japan

Tel: +81-3-3353-8111; Fax: +81-3-5269-9247

E-mail: nagao.michinobu@twmu.ac.jp

Sources of funding for the article:

This research received no specific grant from any funding agency in the public, commercial, or not-for-profit sectors.

Abstract word count: 253 words

Manuscript word count: 4,608 words

Abstract

Objective

Heart transplant rejection leads to cardiac allograft vasculopathy (CAV). ^{13}N-ammonia positron emission tomography (PET) can be useful in detecting CAV, as it can evaluate both epicardial vessels and microvasculature. In this study, we evaluated the regional wall motion in heart transplant patients using our PET-specific feature-tracking (FT) algorithm for myocardial strain calculation and validated it using a cardiovascular magnetic resonance (CMR) FT strain as a reference.

Methods

A total of 15 heart transplant patients who underwent both ^{13}N-ammonia PET and CMR within 3 months were retrospectively enrolled. The same slice position of short-axis cine images of the middle slice of left ventricle (LV) and the same slice position of horizontal long-axis cine images were selected for the two modalities to measure the circumferential strain (CS) and longitudinal strain (LS), respectively. Based on the FT technique, time-strain curves were calculated by semi-automatic tracking of the endocardial contour on cine images throughout a cardiac cycle. The peak value in the time-strain curve was defined as the representative value. Correlations of CS and LS between PET and CMR were analyzed using Pearson correlation coefficients. The inter-modality error of strain measurements was evaluated using intraclass correlation coefficients (ICCs) with two-way random single measures.

Results

Excellent correlations of CS and LS between PET and CMR were observed (CS: $r = 0.80$; $p < 0.01$; LS: $r = 0.87$; $p < 0.01$). Excellent ICCs were observed (0.89 and 0.85) in CS and LS

derived from PET.

Conclusions

We propose the first PET strain showing an excellent agreement with the CMR strain and high reproducibility in measurement.

Keywords

^{13}N-ammonia PET, Cardiac strain, Feature tracking, Cardiac magnetic resonance imaging, Heart transplantation

Introduction

^{13}N-ammonia positron emission tomography (PET) allows for the calculation of the absolute values of myocardial blood flow and myocardial flow reserve (MFR) based on the ratio of myocardial blood flow during coronary artery vasodilation and at rest [1–5]. After heart transplantation, any rejection results in persistent coronary artery inflammation and vascular injury progression, known as cardiac allograft vasculopathy (CAV). Therefore, ^{13}N-ammonia PET is reportedly useful in detecting CAV, as it can evaluate both epicardial vessels and microvasculature [6]. According to the Registry of the International Society for Heart and Lung Transplantation, significant CAV leads to death between 1 and 3 years after transplantation [7]. CAV is asymptomatically accelerated in a denervated transplanted heart. Although experiencing an angina is an important warning sign for heart disease, 70% of heart transplant recipients do not perceive it due to cardiac denervation at the time of heart transplantation [8, 9]. Hence, this lack of early clinical symptoms causes delayed detection of silent myocardial infarction, loss of allograft function, or sudden death [10]. As angiography and intravascular ultrasonography are invasive tests, they pose increased risks to patients [11]. Dobutamine stress echocardiography is currently the most sensitive noninvasive test for cardiac disease [12].

We have developed the world's first PET strain analysis using high-resolution cine imaging with ^{13}N-ammonia PET and feature-tracking (FT) technique [13]. This is a technological innovation with the potential to simultaneously evaluate myocardial blood flow and myocardial motility in a single PET examination. However, ^{13}N-ammonia PET strains have not been compared to strains derived from other conventional techniques, such as cardiovascular magnetic resonance (CMR) FT. In this study, we evaluated the regional

wall motion in heart transplant patients using our PET-specific FT algorithm and validated ^{13}N-ammonia PET strains using CMR FT strains as references. In addition, this study examined the characteristics of regional wall motion in heart transplant patients and the potential for detecting CAV-related wall motion abnormalities using this newly defined technique.

Materials and Methods

Patients

A total of 15 patients who underwent ^{13}N-ammonia PET and CMR examinations after heart transplantation were retrospectively enrolled. PET and CMR scans were performed between April 2018 and March 2021. All patients were >18 years of age at the time of PET scan performance. This retrospective observational study was approved by the appropriate institutional review board and was conducted in accordance with the ethical standards laid down in the 1964 Declaration of Helsinki and all subsequent revisions. Acquisition of written informed consent from patients was waived by the institutional review board. The study results were obtained by retrospective observation. None of the patients had cardiovascular risk factors that were retrieved from the patients' medical records at the time of ^{13}N-ammonia PET.

^{13}N-ammonia PET imaging

After the necessary preparations [14], patients were positioned in a three-dimensional PET system (Biograph mCT; Siemens Healthcare, Erlangen, Germany). Repeatedly upgraded Syngo VA30A_HF07 software was used for dose correction (i.e., the difference

in residual ^{13}N-ammonia activity between resting and stress images). Sequential computed tomography scans (120 kV, 20 mA, and 3-mm slice collimation) were acquired for attenuation correction. Immediately after the intravenous administration of ^{13}N-ammonia (approximately 185 MBq, 5 mCi), ECG-gated image acquisition was performed (10 min at 16 frames/cardiac cycle using the parallel list mode) [15]. After conducting PET myocardial perfusion imaging at rest, the adenosine stress test was carried out at 0.12 mg/kg/min for 6 min. At 3 min after vasodilator administration, ^{13}N-ammonia was infused (approximately 555 MBq, 15 mCi), and myocardial perfusion imaging was performed. Images were reconstructed using Fourier re-binning and filtered back-projection with a 12-mm three-dimensional Hann window for the ramp filter. The reconstructed images were automatically re-orientated to the 16 short-axis, 8 vertical long-axis, and 8 horizontal long-axis cine images. The pixel size of the cine images was 3.2 × 3.2 mm, and the matrix size was 128 × 128, with a 3.0-mm slice thickness. The list mode ^{13}N-ammonia PET data from 2 to 10 min were replayed to reconstruct the ECG-gated images with 16 frames/cardiac cycle [15]. The reconstructed image data with ordered-subsets expectation maximization, point-spread function, and time-of-flight corrections in ^{13}N-ammonia PET, with 21 subsets and four iterations, were transferred to a dedicated software (Syngo MI Cardiology; Siemens Healthcare, Erlangen, Germany). The quantitative gated single-photon emission computed tomography algorithm, developed by Germano et al. [16], was modified for PET to measure the LV volumes and ejection fraction. Mean myocardial and cavity time-activity curves were extracted and polar maps for absolute myocardial blood flow and MFR were generated using dedicated software (Syngo MI Cardiology; Siemens Healthcare, Erlangen, Germany). Myocardial blood flow was determined based on the LV input time-activity

curve and myocardial uptake using a three-compartment model and a dataset of list mode images that were obtained during the first 2 min of imaging of the list mode data. The MFR values based on a 17-segment model of the right coronary artery (RCA), left anterior descending artery (LAD), and left circumflex coronary artery (LCx) territories were determined from the polar maps, as the ratio of the hyperemic myocardial blood flow to resting regional myocardial blood flow [17].

Cine CMR imaging

CMR was performed using a 3.0-Tesla clinical scanner (Ingenia 3.0T; Philips Medical Systems, Best, the Netherlands) equipped with dual-source, parallel radiofrequency transmission and a 32-element cardiac phased coil array for radiofrequency reception. Steady-state free precession images were obtained during the imaging sequence (with patients holding their breath for 10-20 s). Retrospectively, electrocardiogram gating was performed using short-axis views covering the whole left and right ventricles (approximately 10 images each), with 20 phases per cardiac cycle. Three 3 slices of horizontal long-axis cine images were obtained from the middle LV. The following imaging parameters were used in common: repetition time, 3.0 ms; echo time, 2.0 ms; flip angle, 50°; slice thickness, 10 mm; slice gap, 0 mm; field of view, 380 mm × 380 mm; acquisition matrix, 192 × 141; reconstruction matrix, 512 × 512; parallel imaging acceleration factor (SENSE), 2.0. LV volume analysis of CMR was semi-automatically performed with subsequent manual correction using Ziostation 2 software (Ziosoft, Tokyo, Japan). LV volumes and ejection fractions were measured using short-axis images.

Strain analysis with FT

The same image processing algorithms were implemented for resting and stress PET and resting cine CMR using MATLAB R2020a version 9.8 (MathWorks Inc., Natick, MA). These algorithms for PET and CMR imaging have been previously validated [13, 18]. The short-axis slices for strain measurements at the base, middle, and apex of the heart and the horizontal long-axis slice for the middle LV were manually selected. The regional endocardial border was manually defined at end-diastole on the cine images (Fig. 1a). PET images were displayed in gray color (gamma = 1.3) with a standardized uptake value of 10–100%. The endocardium points were evenly spaced based on the line length. In this study, 12 points in the short-axis images and 9 points each in the horizontal and vertical long-axis images were set. The points were then automatically tracked during a cardiac cycle using a local template-matching technique based on normalized correlation coefficient values (Fig. 1b). The template images were automatically based on a square area centered on the following points: the initial size of the template image was set to 24 × 24 pixels and the search area was set to 32 × 32 pixels. The LV endocardial regions were automatically segmented as lines with spline interpolation of the points tracked over a cardiac cycle (Fig. 1c). Finally, the systolic strain values were calculated from the strain curves as the minimum values of the normalized LV regional lengths (Fig. 1d). Systolic strain values from short-axis images were indexed as circumferential strain (CS), and systolic strain values from horizontal long-axis images were indexed as longitudinal strain (LS).

The systolic CS values of three short-axis cine images corresponding to the basal, middle, and apical LV slices were measured using a previously reported 16-segment model

for strain analysis with short-axis images and CMR FT [19]. Global CS was calculated as the mean value of systolic CS for all segments. The regional systolic CS values for the RCA (segments #3, #4, #9, #10, and #15), LAD (segments #1, #2, #7, #8, #13, and #14), and LCx (segments #5, #6, #11, #12, and #16) territories were calculated as the means of systolic strain values at the corresponding segments in the 16-segment model. First, global LS values at the middle LV slice were measured from the lateral wall to the interventricular septum on the horizontal long-axis cine images. Subsequently, global LS was separated into lateral wall and interventricular septum strains, and these were defined as regional LS.

Statistical analysis

All statistical analyses were performed using GraphPad Prism for Mac OS version 8.1.2 (GraphPad Software, La Jolla, CA). Differences were considered statistically significant at $p < 0.05$. The Shapiro–Wilk test was used to evaluate the normality of data distribution, and the means and standard deviations were calculated. Correlations of systolic strain values (CS and LS) between PET and CMR were analyzed using Pearson or Spearman correlation coefficients (r or r_S). Similarly, correlations of LV volumes (end-diastolic volume, end-systolic volume, and ejection fraction) between PET and CMR were analyzed. The inter-modality error of strain measurements was evaluated using Bland–Altman analyses. The intraclass correlation coefficients (ICCs) with two-way random single measures (ICC [2,1]) were calculated by the validated MATLAB code [20]. The ICC values were defined as excellent (≥0.75), good (0.60–0.74), moderate (0.40–0.59), or poor (≤0.39). One-way ANOVA with post-hoc comparison of the LV wall at the anterior (segments #1, #7, #13), septum (segments #2, #3, #18, #9, #14), inferior (segments #4, #10,

#15), and lateral (segments #5, #6, #11, #12, #16) territories was conducted for CMR- and PET-derived CS. CMR- and PET-derived LSs at the LV septum and free wall were compared using the unpaired t-test. PET-derived CS and LS were compared between the stress and resting states using the paired t-test. The correlation coefficient values between strain and MFR were calculated. Further, the correlation coefficient value of the CS ratio at stress to resting state and MFR was calculated. Regional CS territories with MFR <2.0 and ≥2.0 were compared [2] using the unpaired t-test, whereas stress and resting CSs were compared using the paired t-test.

Results

Patient characteristics

Table 1 shows the patients' baseline characteristics as well as the LV parameters from PET and CMR. All CMR scans were performed within 3 months after the latest PET scan. PET-derived LV volumes at end-diastole and end-systole were significantly smaller than those derived from CMR. PET-derived LV ejection fraction was significantly greater than that derived from CMR. PET-derived CSs at ventricular base and apex were unchanged as compared to those derived from CMR, but the PET-derived absolute CS value at middle LV was slightly larger than CMR-derived CS. PET-derived LS had a larger absolute value than that derived from CMR. Overall, 10, 3, and 2 patients had non-significant, mild, and moderate CAV, respectively, according to the International Society for Heart and Lung Transplantation classification [21].

Agreements of strain measurements of PET with CMR

Fig. 2a-d shows scatter plots of the strain values (left column) and Bland–Altman plots (right column). Plots generated from PET-derived and CMR-derived basal CS, middle CS, apical CS, and LS are arranged from top to bottom, respectively. Table 2 shows the agreement between the parameters of LV strains and LV volumes. Correlation coefficients were 0.69–0.81 ($p < 0.01$ for all). Excellent agreements for ICCs were observed (0.75–0.89) in the middle CS, apical CS, and LS, along with a good ICC of basal CS.

Characteristics of regional wall motion in heart transplantation

Fig. 3 shows box-whisker plots of regional CS measured from PET and CMR at the LV anterior, septum, inferior, and lateral regions. No differences in regional PET-derived CSs were identified. Septum CS derived from CMR had a larger absolute value than other regions ($p < 0.01$ for all). Colored CS maps with LV 16-segments demonstrated a large absolute value of strain at the septal region in both PET and CMR (Fig. 4). Fig. 5 shows the box-whisker plots of regional LS measured by PET and CMR at the lateral wall and interventricular septum. PET-derived LS at the lateral wall had a larger absolute value than that at the interventricular septum ($p = 0.03$). There were no differences in CMR-derived LS between the lateral wall and interventricular septum.

Comparison of PET-derived strains between stress and resting state

PET-derived absolute values of anterior CS and lateral CS were increased in the stress state compared to the resting state (Fig. 3a). There were no significant differences in CS in the inferior and septum regions between the stress and resting states. In the comparison of LS, absolute values of stress strains in both the free wall and septum regions

were significantly increased relative to those in the resting state.

Correlation between CSs and MFRs

Table 3 shows correlation coefficients between CSs and MFRs. No correlations were observed with global and regional MFRs with respect to PET-derived CSs and to CMR-derived CSs, respectively. There were no significant correlations between the CMR ratios at stress to resting state, but the LAD CS ratio was moderately correlated to LAD MFR (p = 0.04). No significant differences in both stress and resting CS were observed between territories with MFR <2.0 and ≥2.0 (resting: –25.4±5.2% vs. –26.6±5.1%, p = 0.46; stress: –29.6±6.9% vs. –29.9±5.8%, p = 0.86). In territories with MFR ≥2.0, the absolute value of stress CS was significantly increased, as compared to resting CS (p = 0.006). In contrast, in territories with MFR <2.0, the absolute value of stress CS was moderately increased, as compared to resting CS (p = 0.013).

Discussion

In the present study, the analyses with the correlation coefficients, Bland–Altman analysis, and ICC showed high agreement between PET- and CMR-derived strains. Reported agreements of correlation coefficients, bias with Bland–Altman analysis between echocardiography-derived strains and CMR-derived strains are about 0.7 to 0.8% and -5% to -10%, respectively [22, 23]. Compared to these previous reports, it is reasonable to conclude that PET-FT can provide clinical information regarding myocardial strain. Only a good ICC of basal CS was observed. This is considered to be caused by the different slice thicknesses of the PET and CMR. At the base of the ventricle, the myocardium contracts

significantly in the longitudinal direction as it is pushed out by the dilation of the atrium. We believe that the effect of slice-plane motion affected the agreement of strain measurements using images with different slice thicknesses [24]. PET-derived CS in the inferior wall tended to indicate larger variation (Figure 3a), which is caused by the blurring of myocardial boundaries due to liver accumulation [13]. Therefore, this tendency was not observed in the CS with CMR (Figure 3b). The tracking algorithm for PET imaging may need improvement for accurate assessment in the inferior wall. PET-derived EF and ventricular volume are useful clinical indicators that reflect the global function of the LV [25]. On the other hand, LV volume measurement by PET was underestimated, as compared to CMR. Consequently, LV ejection fraction was overestimated by 20%, particularly due to the large overestimation at end-diastole. The degradation of myocardial motion caused by ischemia is often observed in coronary territories with significant stenosis. We believe that our proposed PET-FT can provide information on regional motion abnormalities induced by ischemia. The resting motion of the transplanted heart was characterized by the largest absolute value of strain of the septum on both PET and CMR images. This feature was evident in the CMR images (Figs. 3 and 4). Heart transplantation results in the loss of fixation of the heart due to pericardial resection. We think this is due to the loss of LV torsion and the increased left-to-right swing of the ventricular septum and free wall. The great septal strain is consistent with a previous echocardiography study [26]. However, the LV ejection fraction was preserved and its pathological significance was noted.

Traditionally, CAV-induced myocardial ischemia is an important factor for predicting the prognosis of patients after heart transplantation. As PET can be used to calculate the

myocardial blood flow and MFR, it is therefore highly sensitive in detecting CAV. Recently, strain measurement by PET-FT had revealed that the absolute value of strain increases during adenosine stress in the normal myocardium but decreases in the ischemic myocardium [13]. However, no association between strain and MFR in the heart transplant patients was identified in this study. Nakamura, et al. calculated the difference of CMR-derived CS between stress and resting state [27]. Because the MFR is defined as the ratio of myocardial blood flow during stress and at resting state, we analyzed the correlation between the CS ratio and MFR in this study. However, no significant association was observed between the two PET-derived parameters. In both myocardium with an MFR of <2.0 and myocardium with an MFR of ≥2.0, an increase in the absolute strain value under adenosine stress was noted. The CS had a significantly larger absolute value for territories with MFR ≥2.0 than those with MFR <2.0. Adenosine decreases peripheral vascular resistance and dilates the capillary bed from arterioles, thereby increasing the myocardial blood flow. A reduction in the absolute strain value caused by adenosine stress is observed in territories with significant stenosis in the epicardial coronary artery. In heart transplant recipients, microcirculatory disturbances occur at an early stage when there is no epicardial coronary stenosis. Decreased MFR reflects this microcirculatory disturbance but does not result in reduced regional wall motion when there is no significant stenosis of the epicardial coronary artery. We speculate that this is the cause of the discrepancy between the strain and the MFR. Thus, combined strain PET analysis is useful for estimating the CAV stage and subsequent treatment strategies.

We acknowledge the limitations of this study, which is the small number of patients due to the single-center retrospective design. However, PET and CMR examinations are not

routinely performed on the same patient, except after heart transplantation, and it is difficult to prepare a large cohort considering the limited number of cases of heart transplantation. The Bland-Altman analysis shows that most of the dots lower than -20% of the mean tend to locate over the blue line. When the myocardium moves quickly and largely, the myocardial contour becomes blurred on PET, and the edge of the myocardial contour are shortened and extracted. This is thought to be the cause of the smaller absolute strain values in PET. Our present research could at least reveal the agreement in CMR- and PET-derive myocardial strain using the same FT algorithm. This suggests that there is a possibility that PET images can be analyzed using commercially available CMR software. Further, our proposed FT algorithm can be potentially applied to single photon emission tomography imaging in future research to further enhance image quality such as that achieved by cadmium-zinc-telluride cameras. Therefore, we believe that this study provides evidence for conducting future multicenter prospective studies using commercial software.

In conclusion, this study characterizes the regional myocardial motion in patients after heart transplantation. It also indicates the possibility of simultaneous evaluation of CAV-related ischemia and LV myocardial motion with PET by comparing it to a CMR-derived strain in the same patients.

Acknowledgments

The authors thank Editage (www.editage.com) for English language editing.

Conflict of interest

The authors have no conflict of interest to declare.

Author contributions

MK and MN contributed to the initial design of the project. All authors contributed to the study conception and design. Material preparation, data collection and analysis were performed by MN, NK and AY. All authors contributed to the interpretation of the data. The first draft of the manuscript was written by MK, and all authors commented and revised previous versions of the manuscript. All authors read and approved the final manuscript.

References

1. Carvajal-Juarez I, Monroy-Gonzalez A, Espinola-Zavaleta N, Meave-Gonzalez A, Alexanderson-Rosas E. PET/CT with ^{13}N-ammonia: characteristics and utility in coronary artery disease. Ann Nucl Cardiol 2019;5:63-8.
2. Fiechter M, Ghadri JR, Gebhard C, Fuchs TA, Pazhenkottil AP, Nkoulou RN, et al. Diagnostic value of 13N-ammonia myocardial perfusion PET: added value of myocardial flow reserve. J Nucl Med 2012;53:1230-4.
3. Giubbini R, Peli A, Milan E, Sciagr R, Camoni L, Albano D, et al. Comparison between the summed difference score and myocardial blood flow measured by 13N-ammonia. J Nucl Cardiol 2018;2:1621-8.
4. Fathala A, Aboulkheir M, Shoukri MM, Alsergani H. Diagnostic accuracy of 13N-ammonia myocardial perfusion imaging with PET-CT in the detection of coronary artery disease. Cardiovasc Diagn Ther 2019;9:35-42.
5. Herzog BA, Husmann L, Valenta I, Gaemperli O, Siegrist PT, Tay FM, et al. Long-term prognostic value of 13N-ammonia myocardial perfusion positron emission tomography added value of coronary flow reserve. J Am Coll Cardiol 2009;54:150-6.
6. Bravo PE, Bergmark BA, Vita T, Taqueti VR, Gupta A, Seidelmann S, et al. Diagnostic and prognostic value of myocardial blood flow quantification as non-invasive indicator of cardiac allograft vasculopathy. Eur Heart J 2018;39:316-23. doi: 10.1093/eurheartj/ehx683.
7. Hertz MI, Taylor DO, Trulock EP, Boucek MM, Mohacsi PJ, Edwards LB, et al. The Registry of the International Society for Heart and Lung Transplantation: nineteenth official report-2002. J Heart Lung Transplant 2002;21:950-70. doi: 10.1016/s1053-

2498(02)00498-9.

8. Ramzy D, Rao V, Brahm J, Miriuka S, Delgado D, Ross HJ. Cardiac allograft vasculopathy: a review. Can J Surg 2005;48:319-27.
9. Schmauss D, Weis M. Cardiac allograft vasculopathy: recent developments. Circulation 2008;117:2131-41. doi: 10.1161/CIRCULATIONAHA.107.711911.
10. Aranda JM Jr, Hill J. Cardiac transplant vasculopathy. Chest 2000;118:1792-800. doi: 10.1378/chest.118.6.1792.
11. Spes CH, Angermann CE. Stress echocardiography for assessment of cardiac allograft vasculopathy. Z Kardiol 2000;89:IX/50-IX/53. doi: 10.1007/s003920070028.
12. Spes CH, Mudra H, Schnaack SD, Klauss V, Reichle FM, Uberfuhr P, et al. Dobutamine stress echocardiography for noninvasive diagnosis of cardiac allograft vasculopathy: a comparison with angiography and intravascular ultrasound. Am J Cardiol 1996;78:168-74. doi: 10.1016/s0002-9149(96)90391-4.
13. Kawakubo M, Nagao M, Yamamoto A, Nakao R, Matsuo Y, Fukushim K, et al. ^{13}N-ammonia positron emission tomography-derived endocardial strain for the assessment of ischemia using feature-tracking in high-resolution cine imaging. J Nucl Cardiol 2021. doi: 10.1007/s12350-021-02677-9.
14. Nakao R, Nagao M, Yamamoto A, Fukushima K, Watanabe E, Sakai S, et al. Papillary muscle ischemia on high-resolution cine imaging of nitrogen-13 ammonia positron emission tomography: association with myocardial flow reserve and prognosis in coronary artery disease. J Nucl Cardiol 2020. doi: 10.1007/s12350-020-02231-z.
15. Dilsizian V, Bacharach SL, Beanlands RS, Bergmann SR, Delbeke D, Dorbala S, et al. ASNC imaging guidelines/SNMMI procedure standard for positron emission

tomography (PET) nuclear cardiology procedures. J Nucl Cardiol 2016;23:1187-226.

16. Germano G, Erel J, Kiat H, Kavanagh PB, Berman DS. Quantitative LVEF and qualitative regional function from gated thallium-201 perfusion SPECT. J Nucl Med 1997;38:749-54.
17. Cerqueira MD, Weissman NJ, Dilsizian V, Jacobs AK, Kaul S, Laskey WK, et al. Standardized myocardial segmentation and nomenclature for tomographic imaging of the heart. J Cardiovasc Magn Reson 2002;4:203-10.
18. Kawakubo M, Arai H, Nagao M, Yamasaki Y, Sanui K, Nishimura H, et al. Global left ventricular area strain using standard two-dimensional cine MR imaging with inter-slice interpolation. Cardiovasc Imaging Asia 2018;2:187-193.
19. Mangion K, Burke NMM, McComb C, Carrick D, Woodward R, Berry C. Feature-tracking myocardial strain in healthy adults- a magnetic resonance study at 3.0 tesla. Sci Rep 2019;9:3239.
20. Arash Salarian (2021). Intraclass Correlation Coefficient (ICC) (https://www.mathworks.com/matlabcentral/fileexchange/22099-intraclass-correlation-coefficient-icc), MATLAB Central File Exchange. Retrieved September 14, 2021.
21. Costanzo MR, Naftel DC, Pritzker MR, Heilman JK 3rd, Boehmer JP, Brozena SC, et al. Heart transplant coronary artery disease detected by coronary angiography: a multiinstitutional study of preoperative donor and recipient risk factors. Cardiac Transplant Research Database. J Heart Lung Transplant 1998;17:744-53.
22. Erley J, Genovese D, Tapaskar N, Alvi N, Rashedi N, Besser SA, et al. Echocardiography and cardiovascular magnetic resonance based evaluation of myocardial strain and relationship with late gadolinium enhancement. J Cardiovasc

Magn Reson 2019;21:46. doi: 10.1186/s12968-019-0559-y.

23. Pryds K, Larsen AH, Hansen MS, Grøndal AYK, Tougaard RS, Hansson NH, et al. Myocardial strain assessed by feature tracking cardiac magnetic resonance in patients with a variety of cardiovascular diseases - A comparison with echocardiography. Sci Rep 2019;9:11296. doi: 10.1038/s41598-019-47775-4.
24. Wu VC, Takeuchi M, Otani K, Haruki N, Yoshitani H, Tamura M, et al. Effect of through-plane and twisting motion on left ventricular strain calculation: direct comparison between two-dimensional and three-dimensional speckle-tracking echocardiography. J Am Soc Echocardiogr 2013;26:1274-81.e4. doi: 10.1016/j.echo.2013.07.006.
25. Khorsand A, Graf S, Eidherr H, Wadsak W, Kletter K, Sochor H, et al. Gated cardiac 13N-NH3 PET for assessment of left ventricular volumes, mass, and ejection fraction: comparison with electrocardiography-gated 18F-FDG PET. J Nucl Med 2005;46:2009-13.
26. Syeda B, Höfer P, Pichler P, Vertesich M, Bergler-Klein J, Roedler S, et al. Two-dimensional speckle-tracking strain echocardiography in long-term heart transplant patients: a study comparing deformation parameters and ejection fraction derived from echocardiography and multislice computed tomography. Eur J Echocardiogr 2011;12:490-6. doi: 10.1093/ejechocard/jer064.
27. Nakamura M, Kido T, Kido T, Tanabe Y, Matsuda T, Nishiyama Y, et al. Quantitative circumferential strain analysis using adenosine triphosphate-stress/rest 3-T tagged magnetic resonance to evaluate regional contractile dysfunction in ischemic heart disease. Eur J Radiol 2015;84:1493-1501. doi: 10.1016/j.ejrad.2015.04.025.

Figure legends

Fig. 1 Semi-automatic strain analysis with feature tracking. The upper images of **a** to **c** are short-axis slices, and the lower images are horizontal long-axis slices. The left column of **a** to **c** shows cardiovascular magnetic resonance images, and the right column shows positron emission tomography images. (**a**) The endocardial borders defined manually at the end of the diastole frame (magenta and green lines). The template images are automatically set, centered by the points on the borders (yellow squares). (**b**) Automatic tracking of the points during the cardiac cycle using a local template-matching technique. (**c**) The endocardial borders are automatically contoured as lines with spline interpolation of the tracked points. (**d**) Calculation of the systolic strain from the strain curves as the minimum values of the normalized regional lengths

Fig. 2 Scatter plots and Bland−Altman plots between PET-derived strains and CMR-derived strains. Graphs of the left column of **a** to **d** are shown as black dotted plots of the strain values. The dashed lines represent approximate lines. Graphs of the right column are shown as Bland–Altman plots. Blue solid lines show bias, and dashed red lines show limits of agreement. Plots of **a** to **d** show the basal, middle, apical, and LS regions, respectively. *PET* positron emission tomography, *CMR* cardiovascular magnetic resonance, *CS* circumferential strain, *LS* longitudinal strain

Fig. 3 Circumferential strains between left ventricular regions. Box–whisker plots of the circumferential strains are shown. PET-derived strains (**a**) and CMR-derived strains (**b**) are

indicated. Regional circumferential strains are anterior, inferior, septum, and lateral, from left to right. **$p < 0.01$, *$p < 0.05$. *PET* positron emission tomography, *CMR* cardiovascular magnetic resonance

Fig. 4 Colored circumferential strain maps according to left ventricular 16-segments model. PET-derived strain maps at resting and stress states (**a** and **b**) and a CMR-derived strain map (**c**) are indicated. Circumferential strains of −20% to −30% are described in blue to red. *PET* positron emission tomography, *CMR* cardiovascular magnetic resonance

Fig. 5 Longitudinal strains between left ventricular regions. Box–whisker plots of the longitudinal strains are shown. PET-derived strains (**a**) and CMR-derived strains (**b**) are indicated. The regional longitudinal strains are the free wall and septum (left and right, respectively). **$p < 0.01$, *$p < 0.05$. *PET* positron emission tomography, *CMR* cardiovascular magnetic resonance

Figure

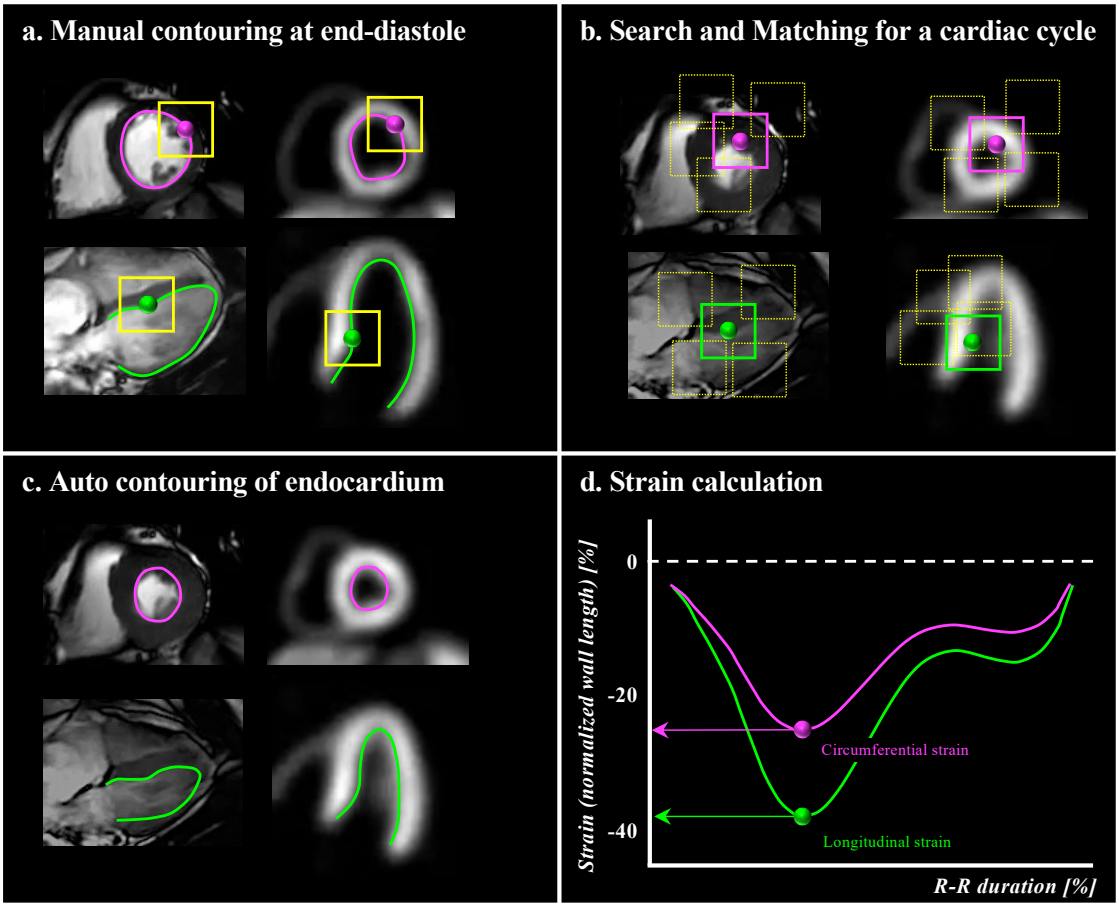

Fig. 1 Semi-automatic strain analysis with feature-tracking

The upper images of a to c are short-axis slices, and the lower images are horizontal long-axis slices. The left column of a to c shows cardiovascular magnetic resonance images, and the right column shows positron emission tomography images.

(a) The endocardial borders defined manually at the end of the diastole frame (magenta and green lines). The template images are automatically set, centered by the points on the borders (yellow squares). (b) Automatic tracking of the points during the cardiac cycle using a local template-matching technique. (c) The endocardial borders are automatically contoured as lines with spline interpolation of the tracked points. (d) Calculation of the systolic strain from the strain curves as the minimum values of the normalized regional lengths.

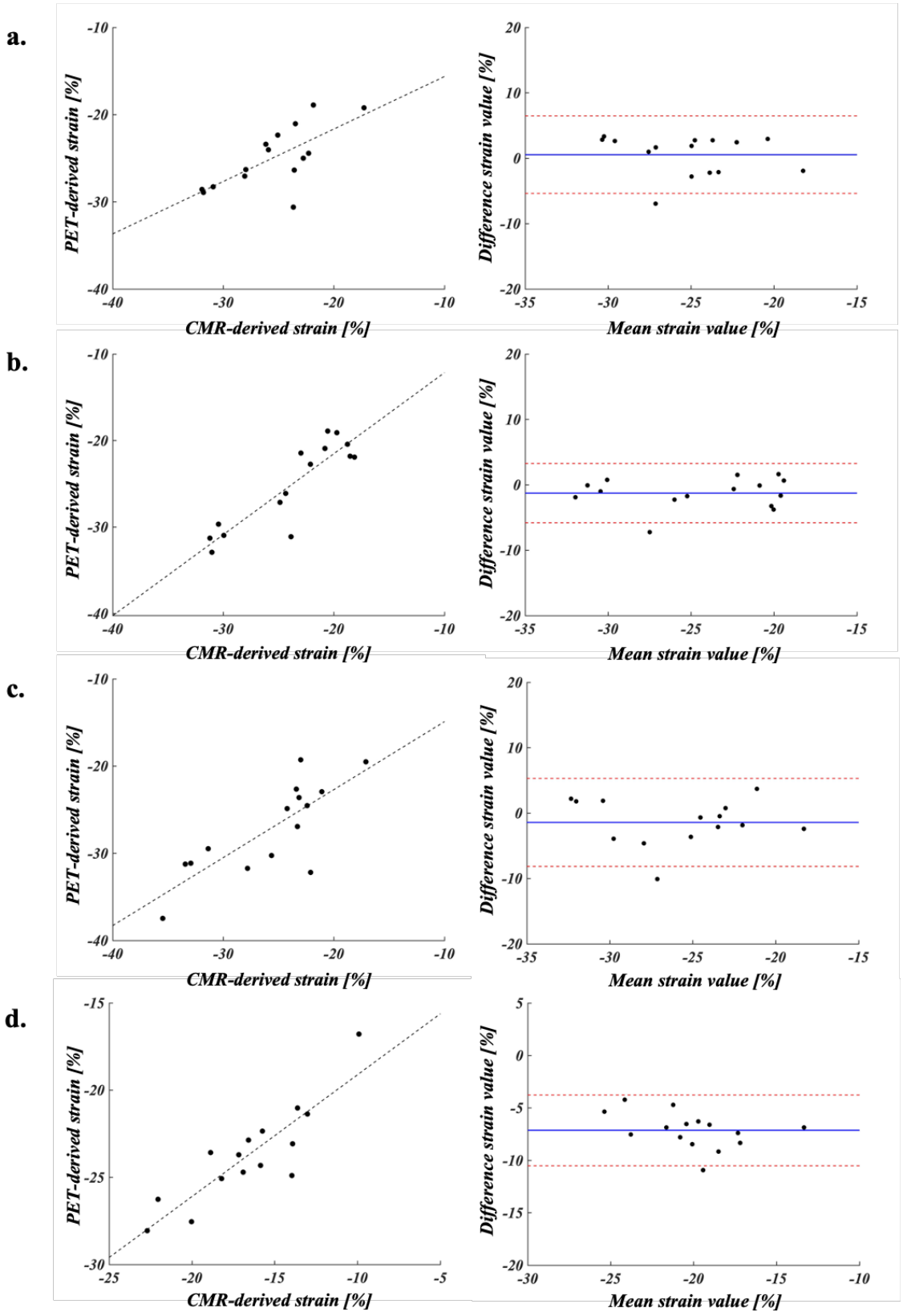

Fig. 2 Scatter plots and Bland−Altman plots between PET-derived strains and CMR derived strains

Graphs of the left column of a to d are shown as black dotted plots of the strain values. The dashed lines are indicated as approximate lines. Graphs of the right column are shown as Bland–Altman plots. Blue solid lines show bias, and dashed red lines show limits of agreement.

Plots of a to d show the basal, middle, apical, and LS regions, respectively.

PET, positron emission tomography; CMR, cardiovascular magnetic resonance; CS, circumferential strain; LS, longitudinal strain.

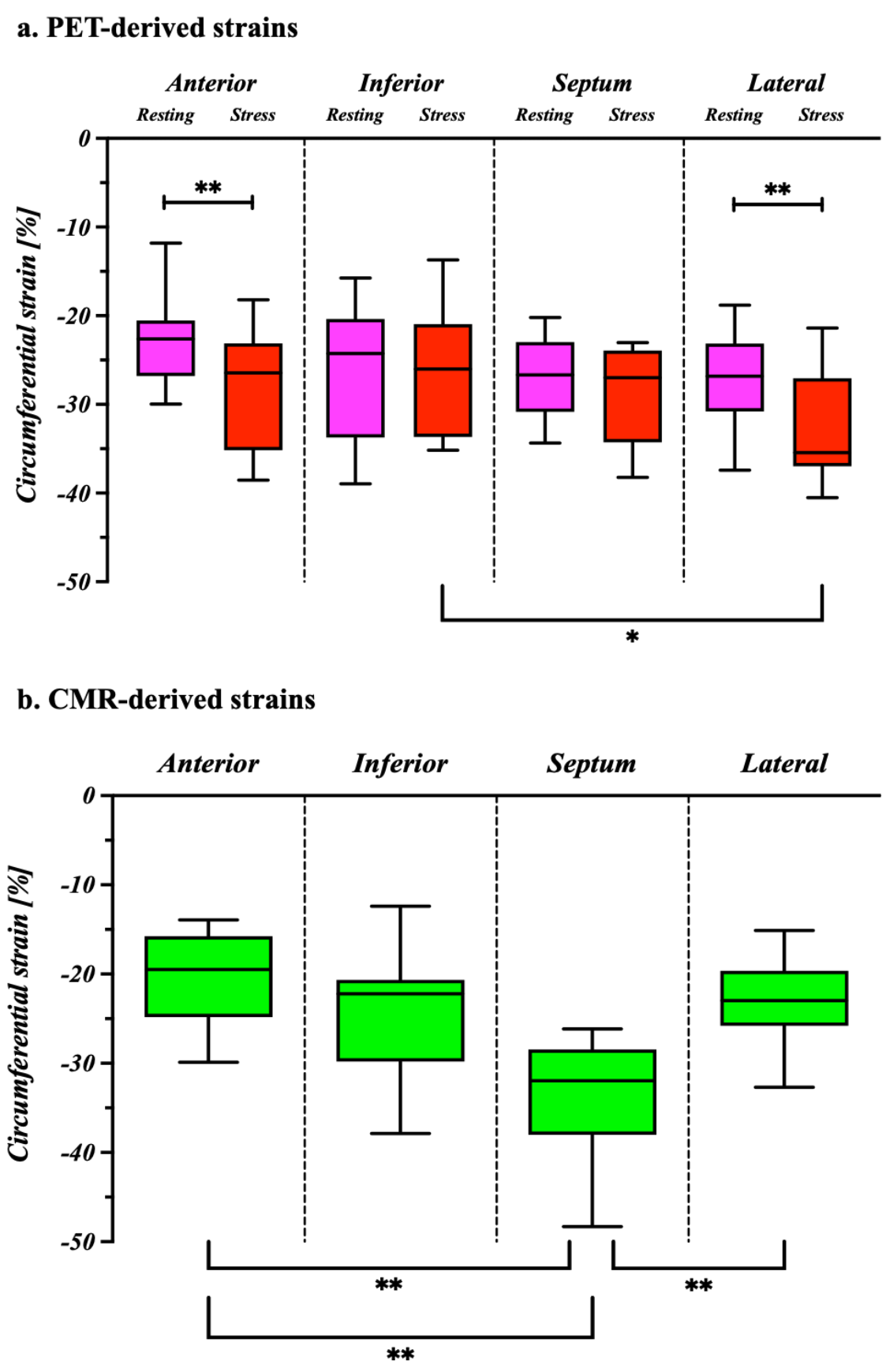

Fig. 3 Circumferential strains between left ventricular regions

Box–whisker plots of the circumferential strains are shown. PET-derived strains (a) and CMR-derived strains (b) are indicated. Regional circumferential strains are anterior, inferior, septum, and lateral, from left to right.

$^{**}p<0.01$, $^{*}p<0.05$. PET, positron emission tomography; CMR, cardiovascular magnetic resonance.

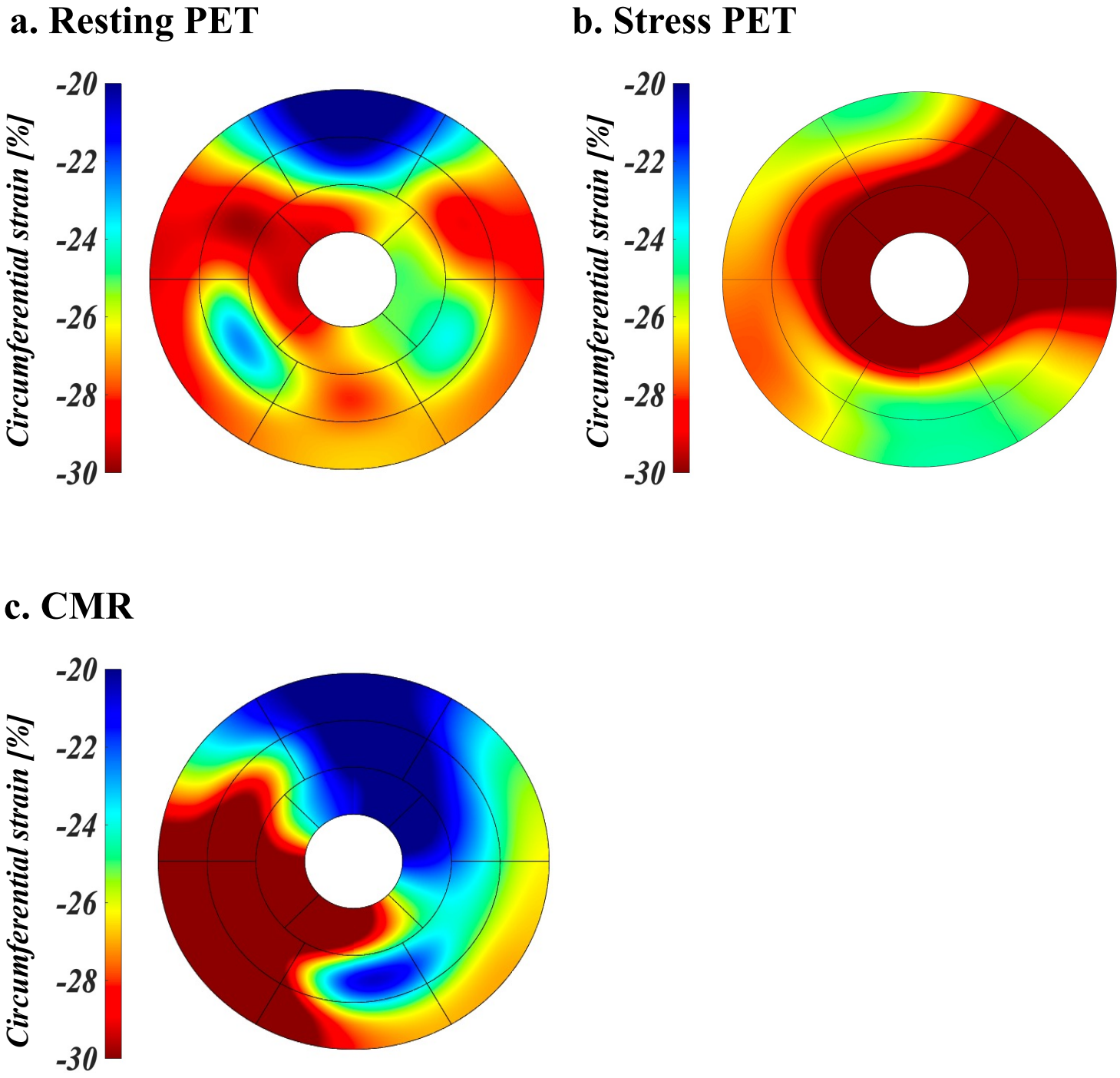

Fig. 4 Colored circumferential strain maps according to left ventricular 16-segments model

PET-derived strain maps at resting and stress states (a and b) and a CMR-derived strain map (c) are indicated. Circumferential strains of −20 % to −30 % are described in blue to red.

PET, positron emission tomography; CMR, cardiovascular magnetic resonance.

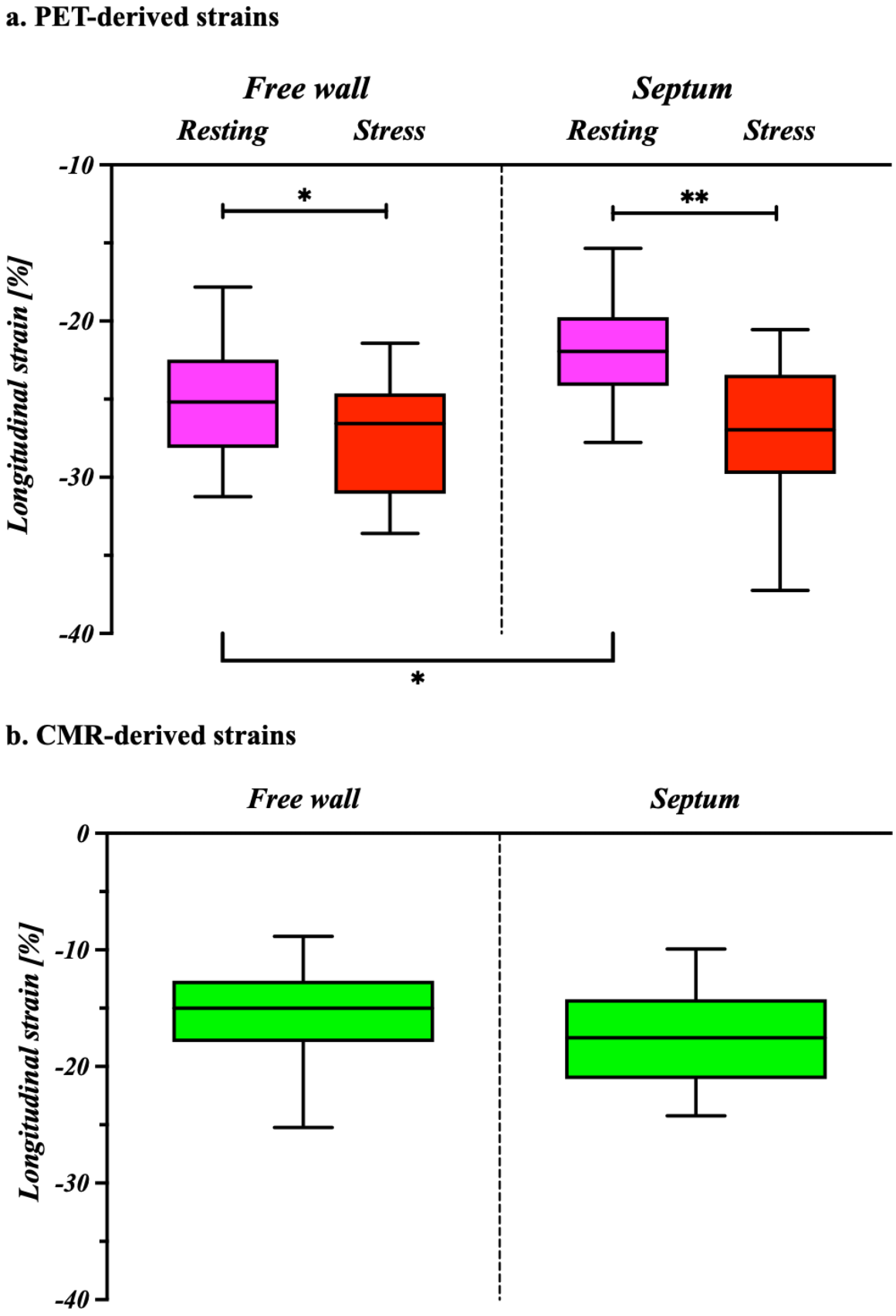

Fig.5 Longitudinal strains between left ventricular regions

Box–whisker plots of the longitudinal strains are shown. PET-derived strains (a) and CMR-derived strains (b) are indicated. The regional longitudinal strains are the free wall and septum (left and right, respectively).

**p<0.01, *p<0.05. PET, positron emission tomography; CMR, cardiovascular magnetic resonance.

Table

TABLE 1 Patient's characteristics, ventricular volume parameters, and strain parameters

Characteristics	Patients after heart transplantation (n = 15)		*P*-value
Male/Female	10/5		–
Age (y)	43 ± 14		–
WHO classification (Ⅰ/ Ⅱ/ Ⅲ/Ⅳ)	10/2/3/0		–
Years after transplantation	12 ± 8		–
Age at the transplantation (<18y/≥18y)	6/9		–
PET to CMR duration (day)	67 ± 23		–
LV volume parameters	PET	CMR	
EDV (mL)	79.5 ± 22.9	92.3 ± 18.3	0.002
ESV (mL)	22.3 ± 10.1	44.9 ± 13.7	<0.0001
EF (%)	72.8 ± 6.3	52.0 ± 6.1	<0.0001
LV strain parameters	PET	CMR	
Basal CS (%)	-25.0 ± 3.4	-25.5 ± 3.9	0.49
Middle CS (%)	-25.1 ± 4.8	-23.8 ± 4.6	0.048
Apical CS (%)	-27.2 ± 5.1	-25.8 ± 5.1	0.13
LS (%)	-22.0 ± 1.6	-16.9 ± 1.9	<0.0001

HR, heart rate; WHO, world health organization; PET, positron emission tomography; CMR, cardiovascular magnetic resonance; LV, left ventricular; EDV, end-diastole volume; ESV, end-systole volume; EF, ejection fraction; CS, circumferential strain; LS, longitudinal strain.

TABLE 2 Parameters of agreement of LV strains and LV volumes

Parameter	LV strains [%]				LV volumes		
	Basal CS	Middle CS	Apical CS	LS	EDV [mL]	ESV [mL]	EF [%]
Correlation coefficients	0.69**	0.80**	0.79**	0.87**	0.80**	0.87**	0.75**
Bias (LOA)	0.6 (–5.4, 6.5)	–1.3 (–5.8, 3.3)	–1.4 (–8.2, 5.3)	–7.1 (–10.5, –3.8)	–12.7 (–35.6, 10.2)	–22.6 (–39.1, –6.1)	20.8 (11.9, –30.0)
SDD	3.0	2.3	3.4	1.7	11.7	8.4	4.5
ICC (95% CI)	0.69 (0.29–0.88)	0.89 (0.70–0.96)	0.79 (0.47–0.92)	0.85 (0.61–0.95)	0.85 (0.62–0.95)	0.77 (0.45–0.92)	0.75 (0.41–0.91)

CI, confidence interval; CS, circumferential strain; EDV, end-diastolic volume; ESV, end-systolic volume; EF, ejection fraction; ICC, intraclass correlation coefficient; LOA, limit of agreement; LV, left ventricular; LS, longitudinal strain; SDD, standard deviation of the difference.

Underlined parameters are normal data distribution.

**$p < 0.01$.

TABLE 3 Correlation coefficients between circumferential strains and myocardial flow reserves

	Stress/Resting Ratio		Stress PET		Resting PET		CMR	
	Correlation coefficients	*P*-value	Correlation coefficients	*P*-value	Correlation coefficients	*P*-value	Correlation coefficients	*P*-value
Global CS vs. Global MFR	0.30	0.28	–0.02	0.94	0.14	0.62	0.21	0.44
RCA CS vs. RCA MFR	–0.05	0.85	0.07	0.80	0.20	0.48	–0.03	0.90
LAD CS vs. LAD MFR	0.53	0.04	–0.20	0.48	0.35	0.20	0.37	0.18
LCx CS vs. LCx MFR	0.32	0.25	0.08	0.77	0.09	0.74	–0.07	0.80

Spearman's correlation analyses due to data non-normal distribution were expressed with underline.

PET, positron emission tomography; CMR, cardiovascular magnetic resonance; CS, circumferential strain, MFR; myocardial flow reserve; RCA, right coronary artery; LAD, left anterior descending artery; LCx, left circumflex coronary artery.